Figure S1

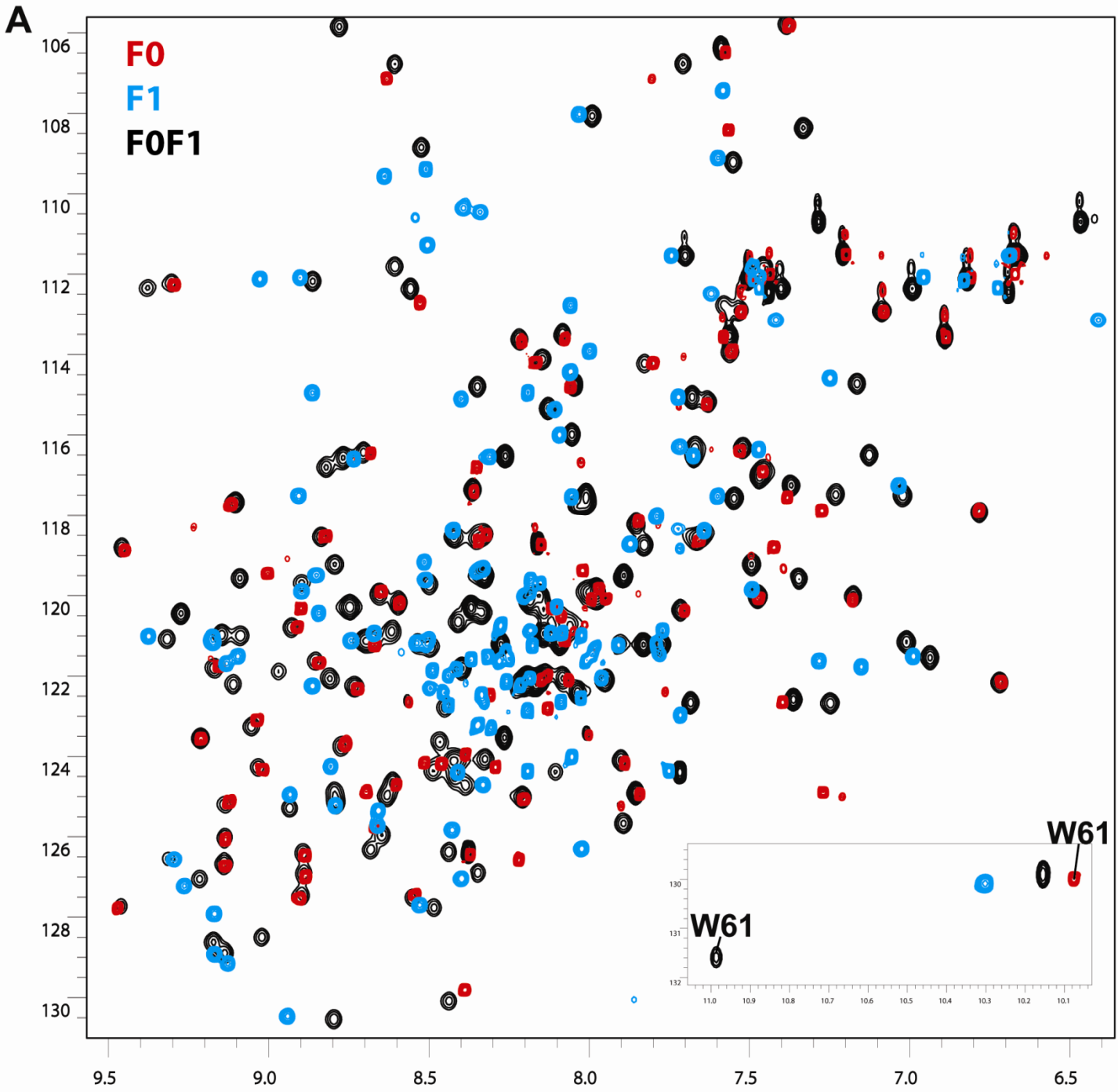
A
F0
F1
F0F1
106
108
110
112
114
116
118
120
122
124
126
128
130
9.5
9.0
8.5
8.0
7.5
7.0
6.5
W61
W61
130
131
132
11.0
10.9
10.8
10.7
10.6
10.5
10.4
10.3
10.2
10.1

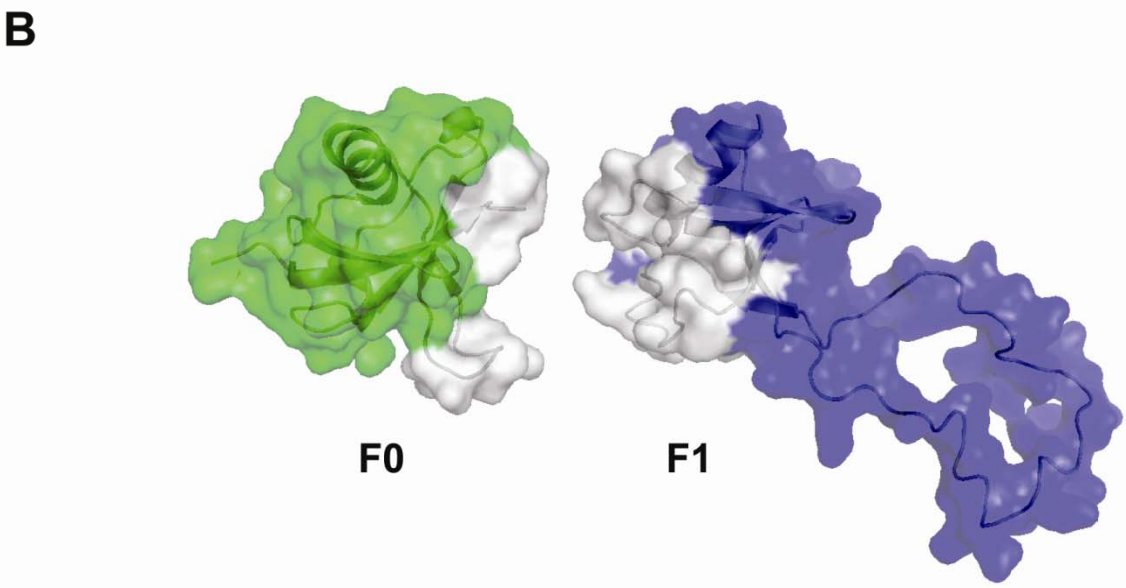
B
F0
F1

Figure S2

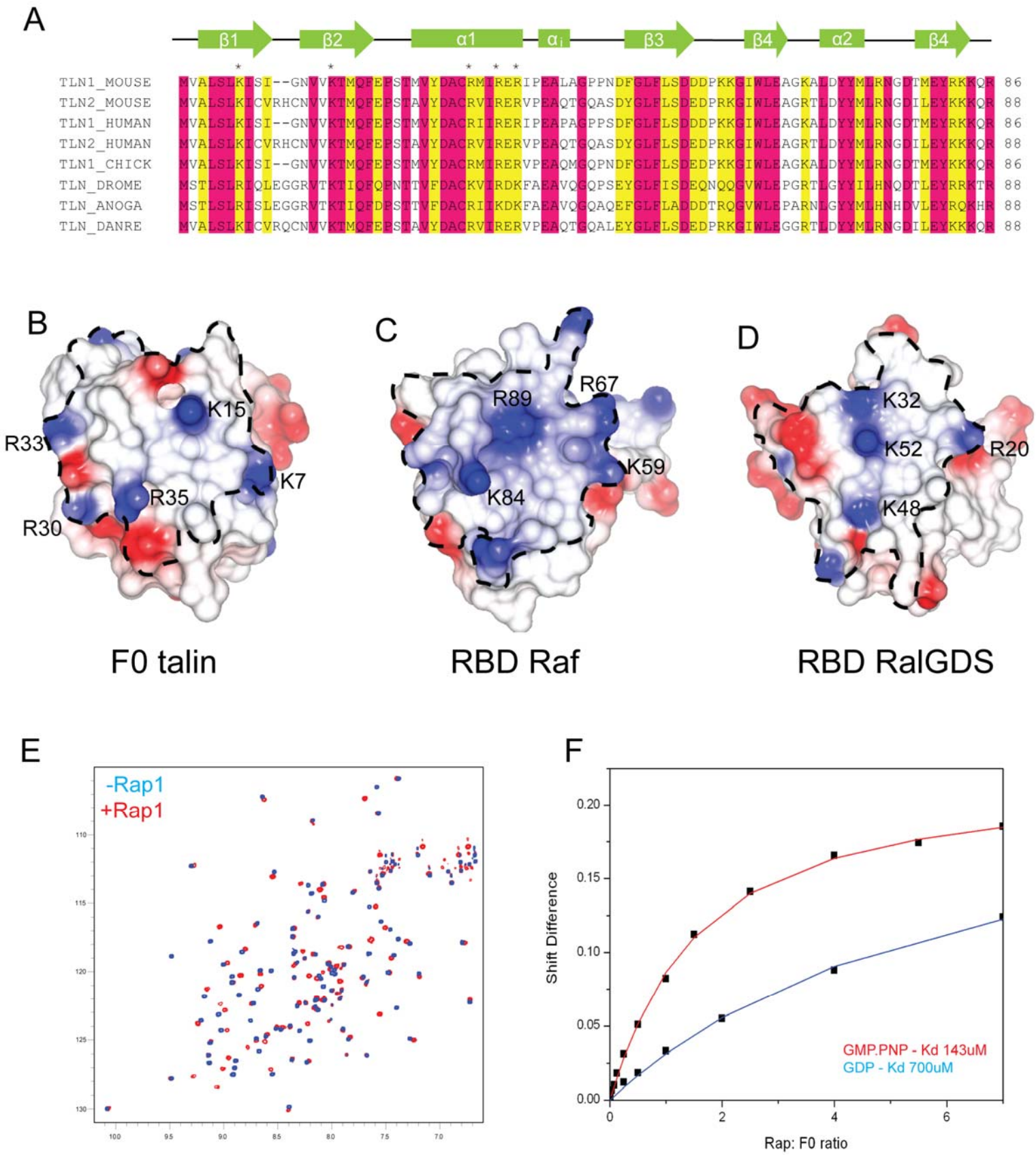
A
β1
β2
α1
α1
β3
β4
α2
β4
TLN1_MOUSE MVALSLKLSI--GNVVKTMQFEPSTMVYDACRMIRERIPEALAGPPNDFGLFLSDDPKKGIWLEAGKALDYYMLRNGDTMEYRKKQR 86
TLN2_MOUSE MVALSLKICVRHCNVVKTMQFEPSTAVYDACRVIRERVPEAQTGQASDYGLFLSDEDPRKGIWLEAGRTLDYYMLRNGDILEYKKKQR 88
TLN1_HUMAN MVALSLKLSI--GNVVKTMQFEPSTMVYDACRIIRERIPEAPAGPPSDFGLFLSDDPKKGIWLEAGKALDYYMLRNGDTMEYRKKQR 86
TLN2_HUMAN MVALSLKICVRHCNVVKTMQFEPSTAVYDACRVIRERVPEAQTGQASDYGLFLSDEDPRKGIWLEAGRTLDYYMLRNGDILEYKKKQR 88
TLN1_CHICK MVALSLKLSI--GNVVKTMQFEPSTMVYDACRMIRERVPEAQMGQPNDFGLFLSDEDPKKGIWLEAGKALDYYMLRNGDTMEYKKKQR 86
TLN_DROME MSTLSLRIQLEGGRVTKTIQFQPNTTVFDACKVIRDKFAEAVQGQPSEYGLFISDEQNQQGVWLEPGRTLGYYILHNQDTLEYRRKTR 88
TLN_ANOGA MSTLSLRLSLEGGRVTKTIQFDPSTTVFDACRIIKDKFAEAVQGQAQEFGLFLADDDTRQGVWLEPARNLGYYMLHNHDVLEYRQKHR 88
TLN_DANRE MVALSLKICVRQCNVVKTMQFEPSTAVYDACRVIRERVPEAQTGQALEYGLFLSDEDPRKGIWLEGGRTLDYYMLRNGDILEYKKKQR 88
B
K15
R33
K7
R35
R30
F0 talin
C
R89
R67
K59
K84
RBD Raf
D
K32
K52
R20
K48
RBD RalGDS
E
-Rap1
+Rap1
110
115
120
125
130
100
95
90
85
80
75
70
F
Shift Difference
0.20
0.15
0.10
0.05
0.00
0
2
4
6
Rap: F0 ratio
GMP.PNP - Kd 143uM
GDP - Kd 700uM

Figure S3

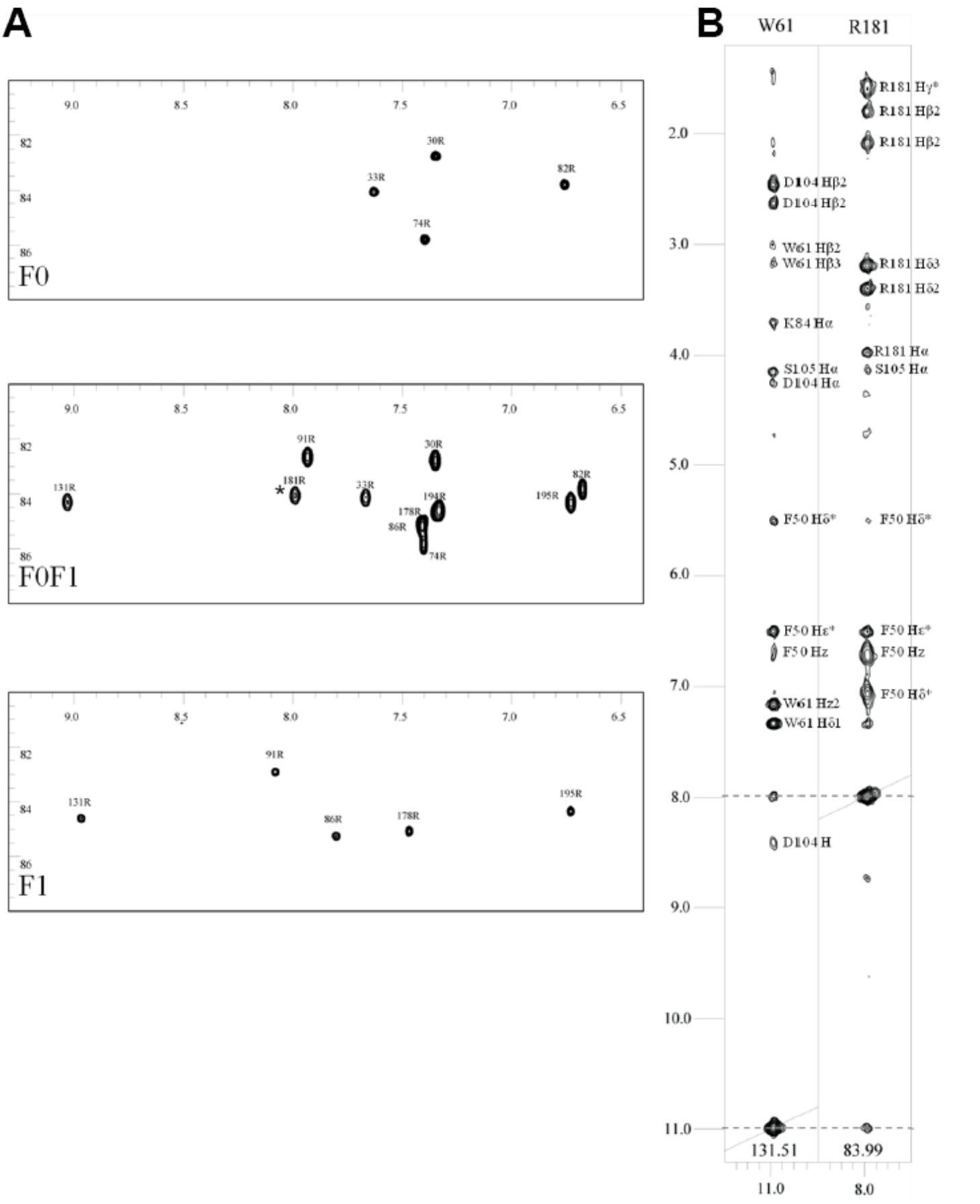
A
F0
F0F1
F1
30R
33R
82R
74R
91R
181R
131R
194R
178R
86R
195R
B
W61
R181
R181 Hγ*
R181 Hβ2
D104 Hβ2
W61 Hβ2
W61 Hβ3
R181 Hδ3
R181 Hδ2
K84 Hα
R181 Hα
S105 Hα
D104 Hα
F50 Hδ*
F50 Hε*
F50 Hz
W61 Hz2
W61 Hδ1
D104 H
131.51
83.99
11.0
8.0

Figure S4

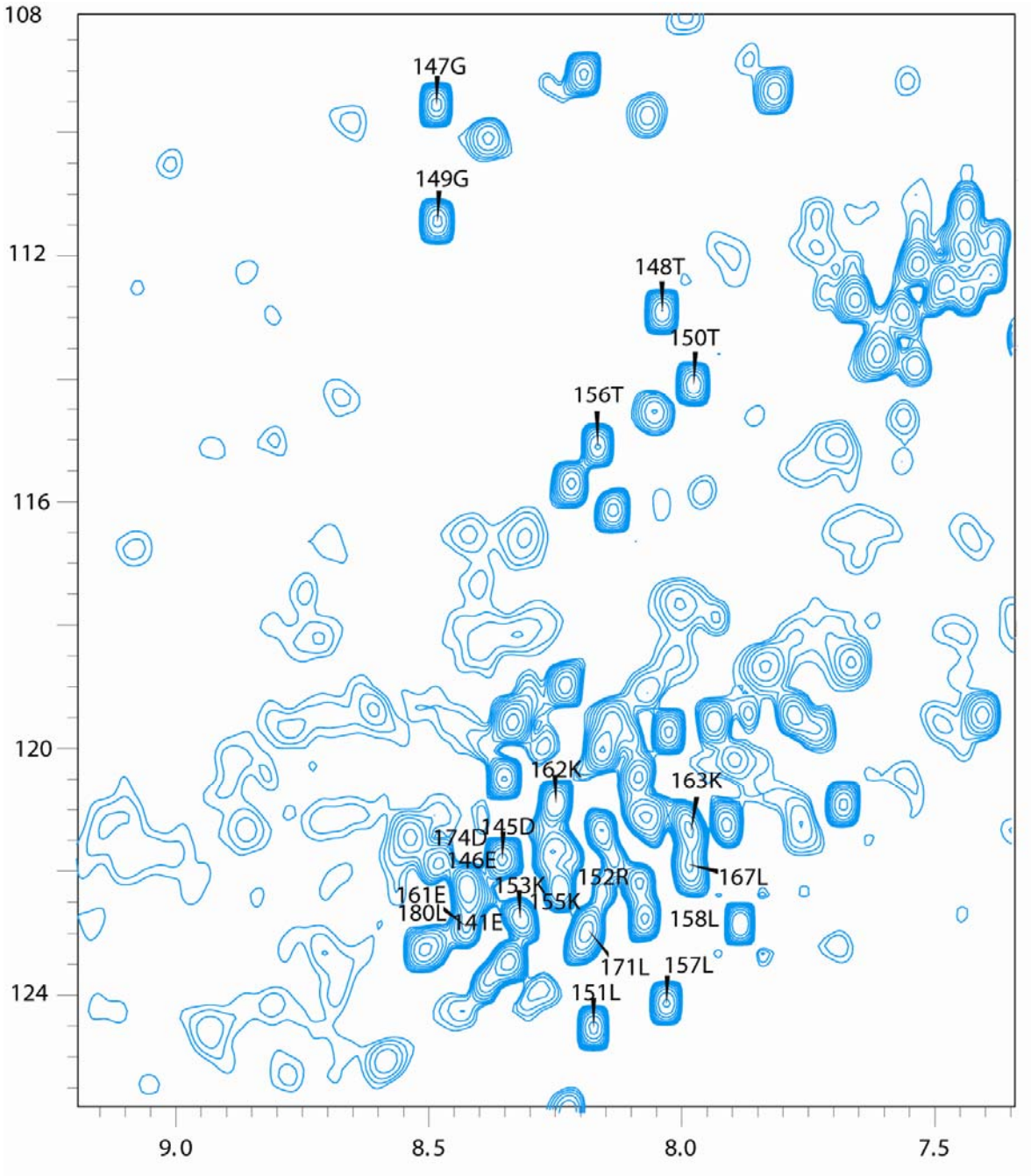
108
112
116
120
124
9.0
8.5
8.0
7.5
147G
149G
148T
150T
156T
162K
163K
145D
174D
146E
153K
152R
167L
161E
155K
180L
141E
158L
171L
157L
151L

Figure S5

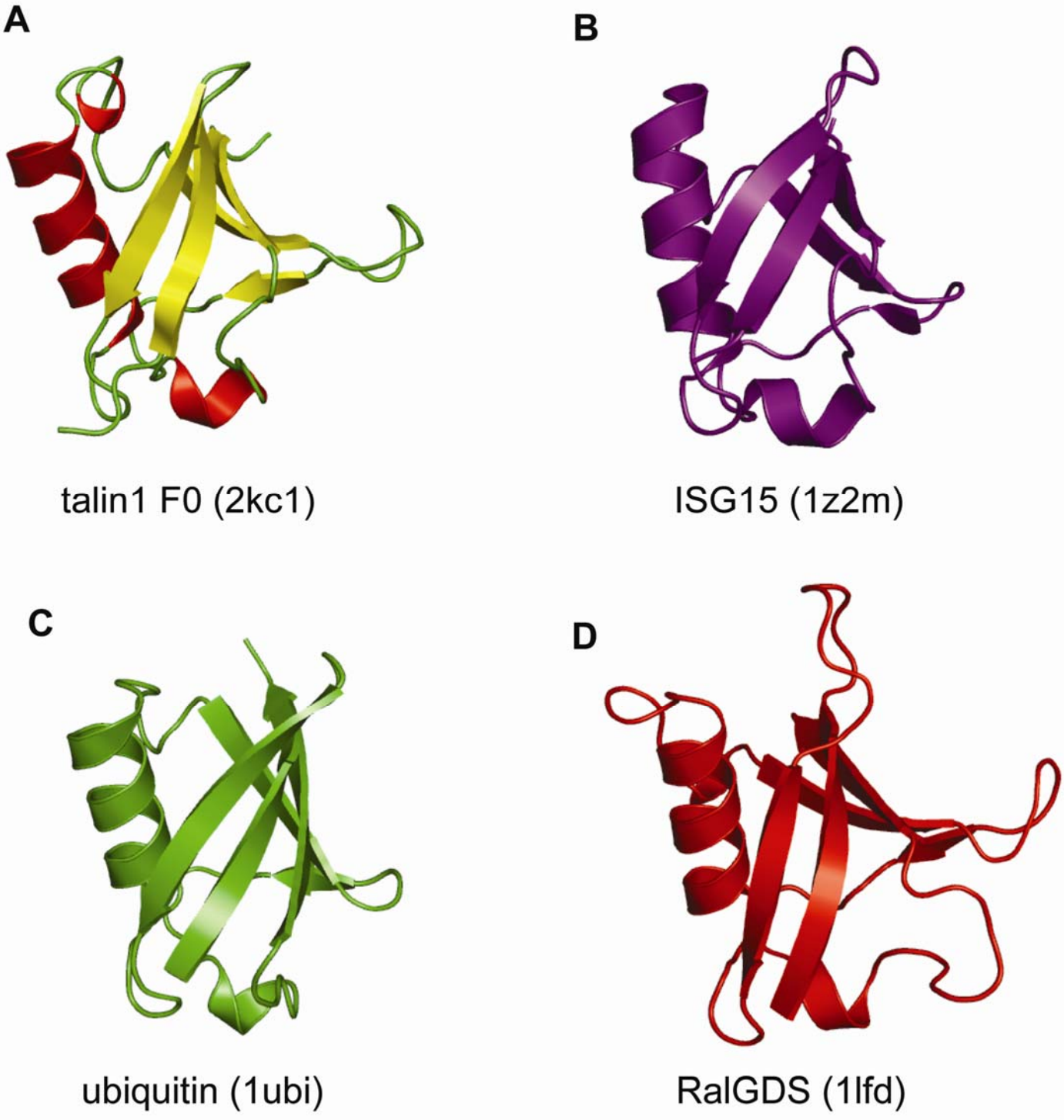

Figure S6

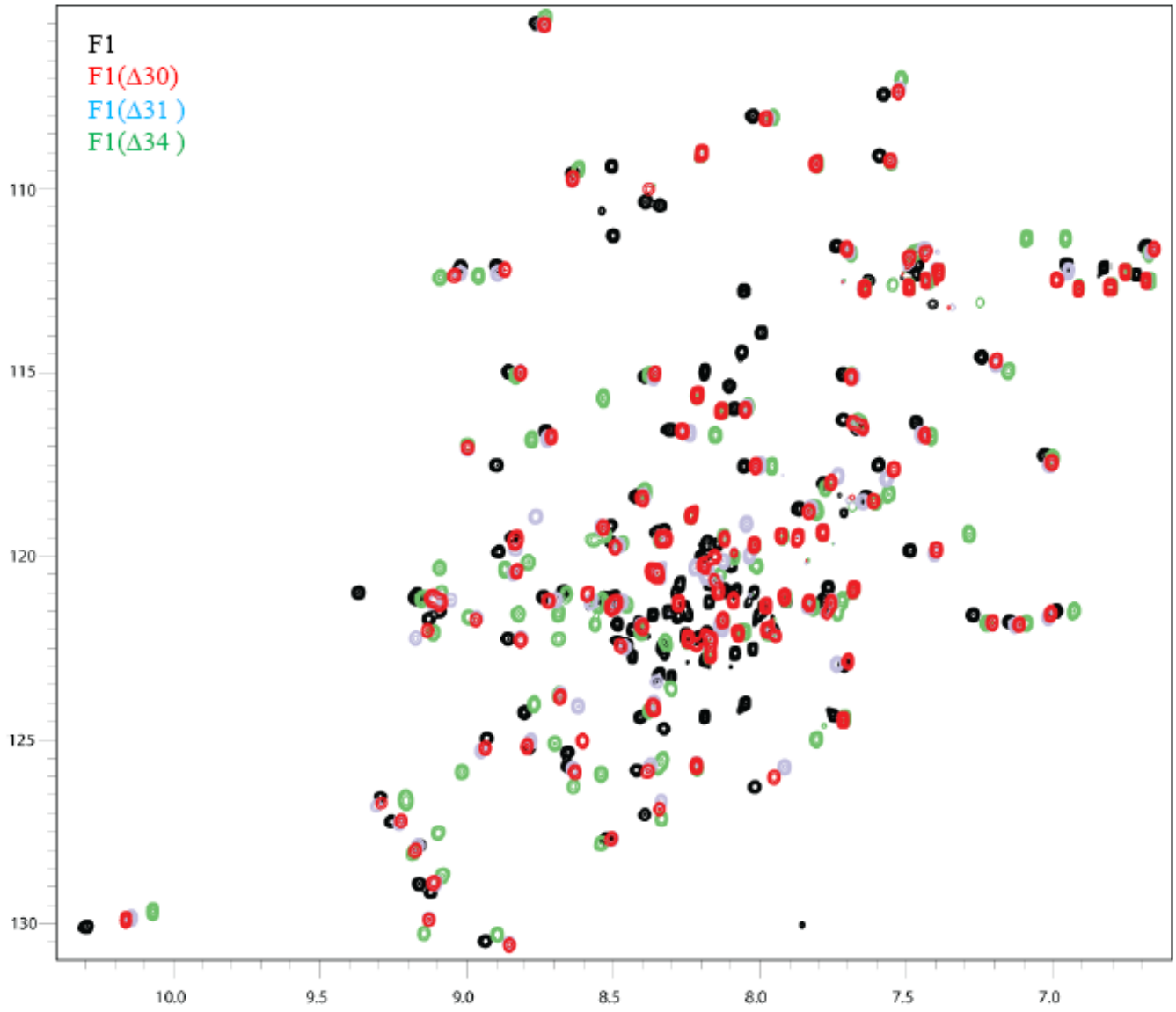

Figure S7

A

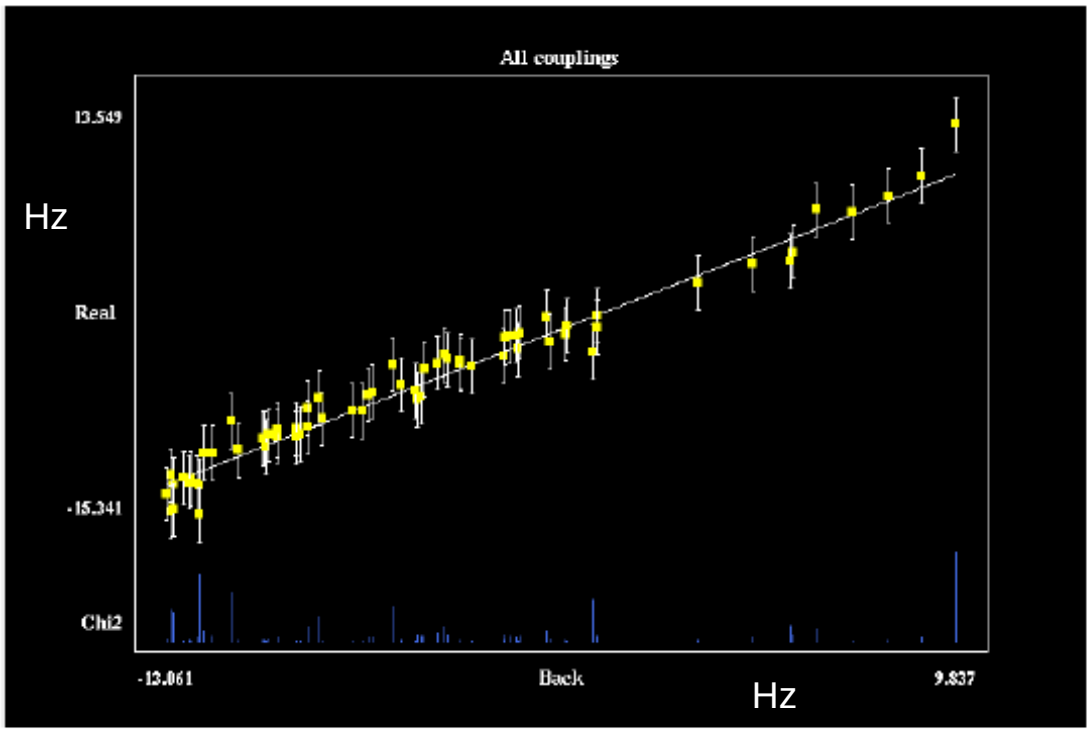
All couplings
13.549
Hz
Real
-15.341
Chi2
-13.061
Back
9.837
Hz

B

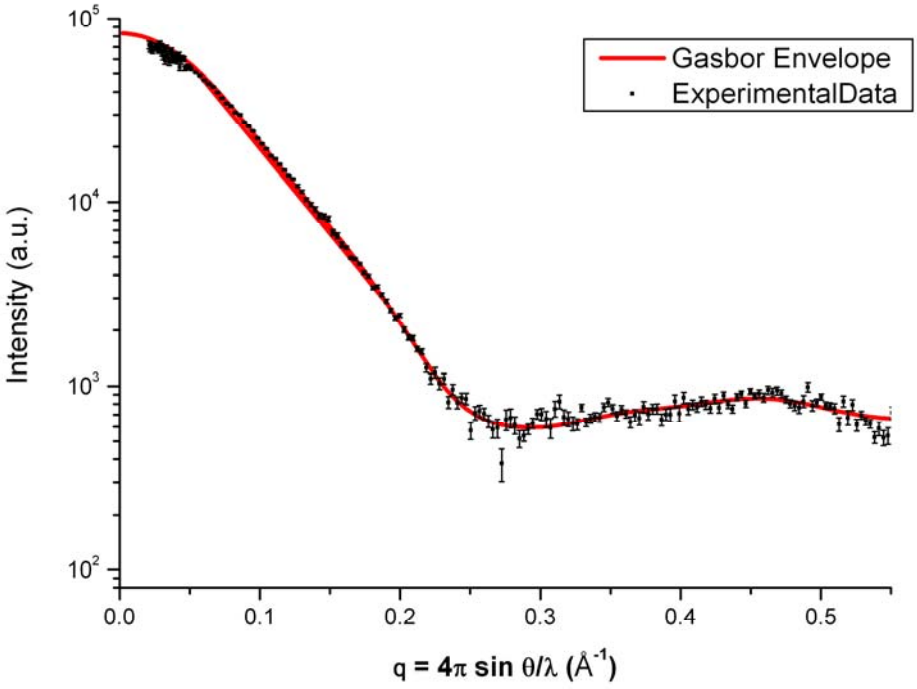
Gasbor Envelope
ExperimentalData
Intensity (a.u.)
10^5
10^4
10^3
10^2
0.0
0.1
0.2
0.3
0.4
0.5
q = 4π sin θ/λ (Å^-1)

Figure S8

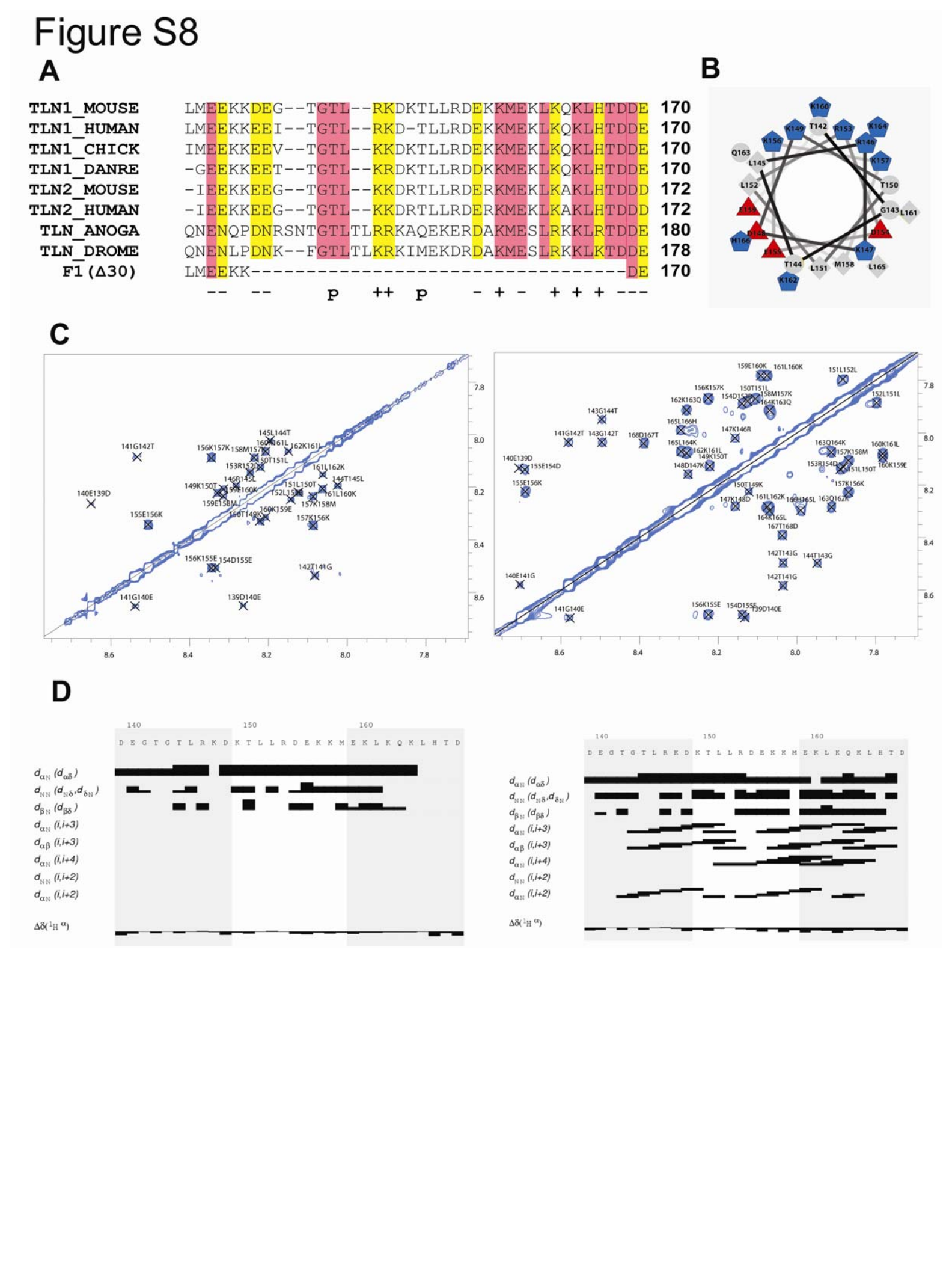
A
TLN1_MOUSE LMEEKKDEG--TGTL--RKDKTLLRDEKKMEKLKQKLHTDDE 170
TLN1_HUMAN LMEEKKEEI--TGTL--RKD-TLLRDEKKMEKLKQKLHTDDE 170
TLN1_CHICK IMEEKKEEV--TGTL--KKDKTLLRDEKKMEKLKQKLHTDDE 170
TLN1_DANRE -GEEKKEET--TGTL--KRDKTLLRDDKKMEKLKQKLHTDDE 170
TLN2_MOUSE -IEEKKEEG--TGTL--KKDRTLLRDERKMEKLKAKLHTDDD 172
TLN2_HUMAN -IEEKKEEG--TGTL--KKDRTLLRDERKMEKLKAKLHTDDD 172
TLN_ANOGA QNENQPDNRSNTGTLTLRRKAQEKERDAKMESLRKKLRTDDE 180
TLN_DROME QNENLPDNK--FGTLTLKRKIMEKDRDAKMESLRKKLKTDDE 178
F1(Δ30) LMEEKK---------- DE 170
-- -- p ++ p - + - + + + ---
B
C
D

Figure S9

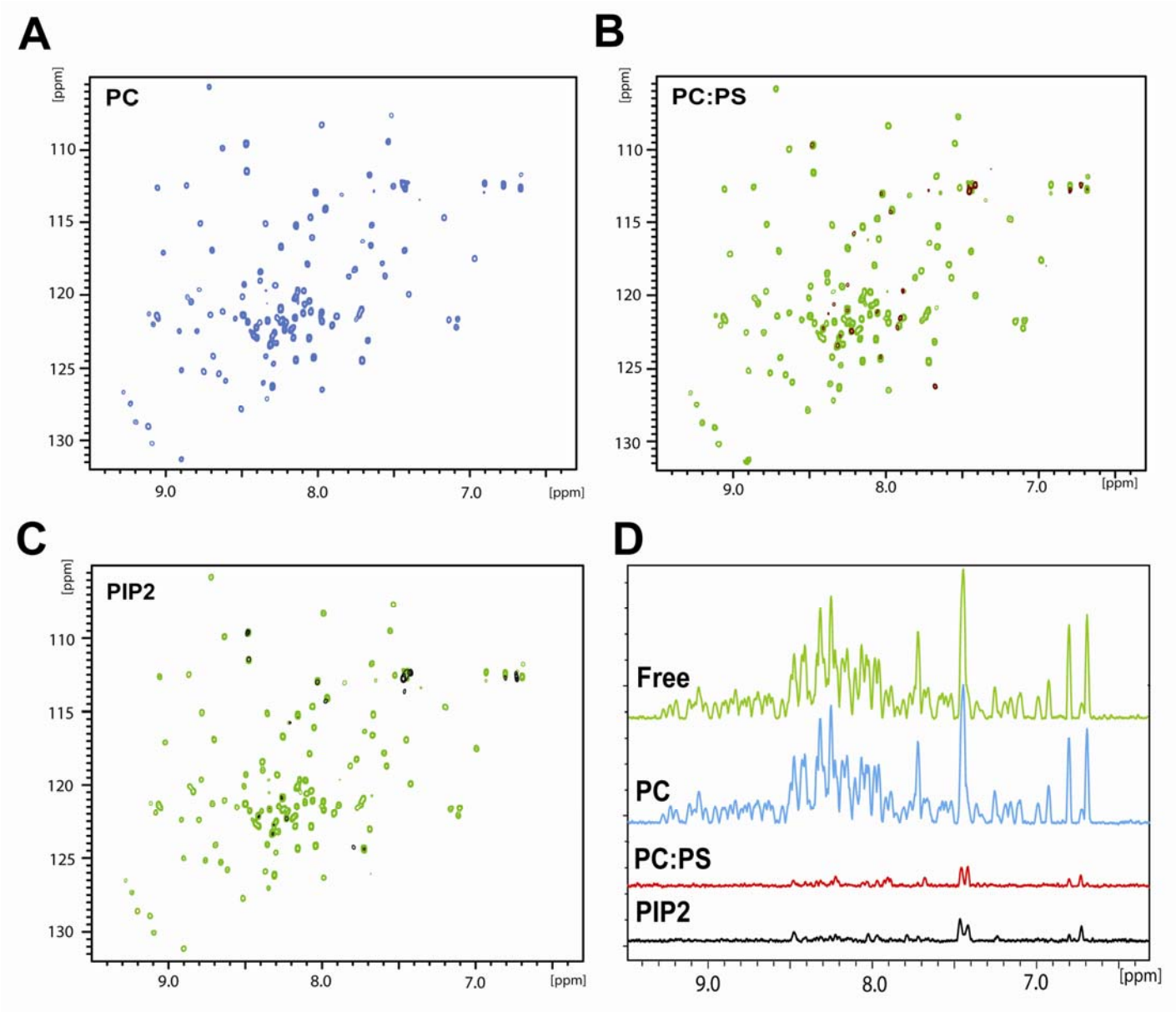
A
PC
[ppm]
110
115
120
125
130
9.0
8.0
7.0
[ppm]
B
PC:PS
[ppm]
110
115
120
125
130
9.0
8.0
7.0
[ppm]
C
PIP2
[ppm]
110
115
120
125
130
9.0
8.0
7.0
[ppm]
D
Free
PC
PC:PS
PIP2
9.0
8.0
7.0
[ppm]

Figure S10

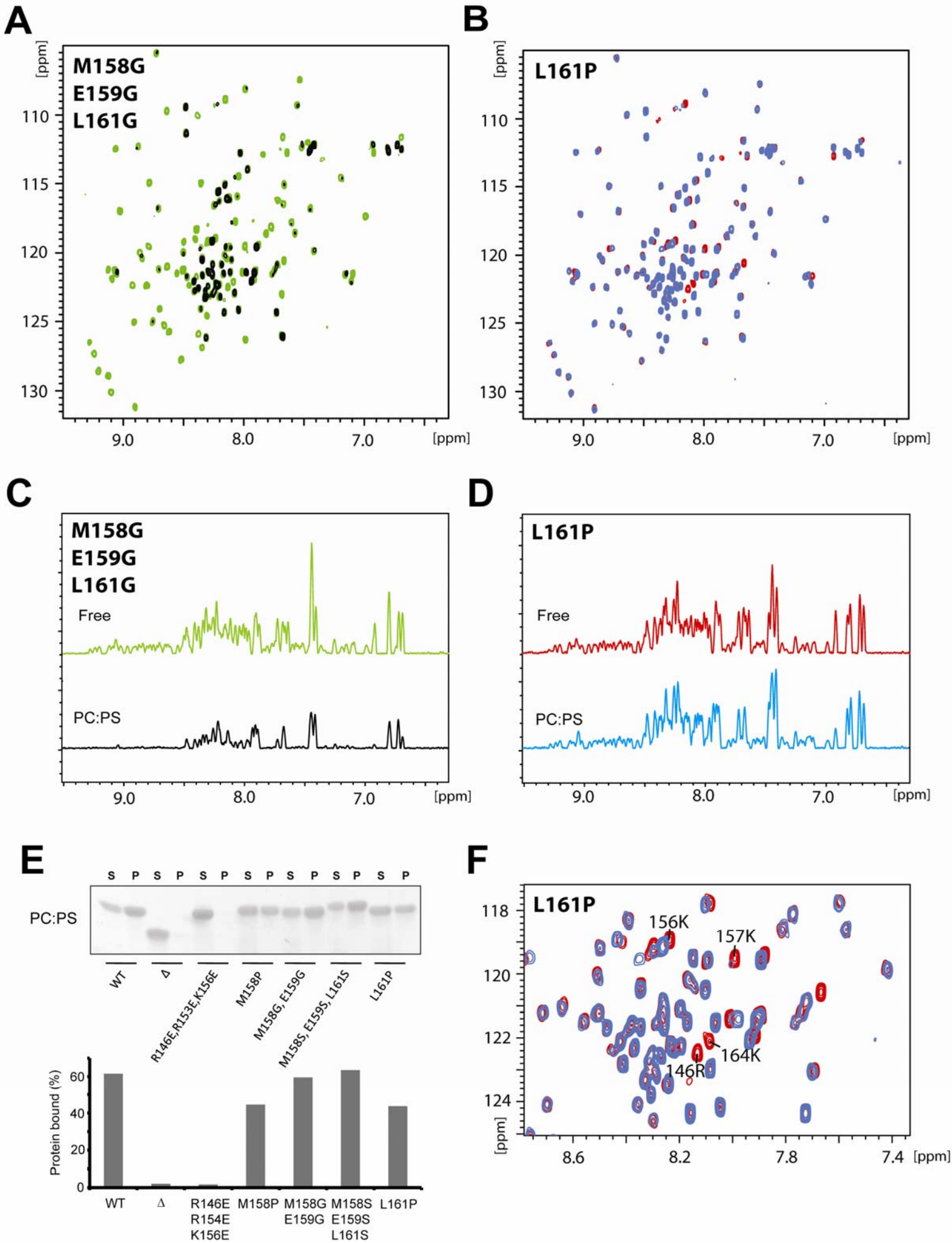
A
M158G
E159G
L161G
[ppm]
110
115
120
125
130
9.0
8.0
7.0
[ppm]
B
L161P
[ppm]
110
115
120
125
130
9.0
8.0
7.0
[ppm]
C
M158G
E159G
L161G
Free
PC:PS
9.0
8.0
7.0
[ppm]
D
L161P
Free
PC:PS
9.0
8.0
7.0
[ppm]
E
S P S P S P S P S P S P S P
PC:PS
WT
Δ
R146E,R153E,K156E
M158P
M158G, E159G
M158S, E159S, L161S
L161P
Protein bound (%)
60
40
20
0
WT
Δ
R146E
R154E
K156E
M158P
M158G
E159G
M158S
E159S
L161S
L161P
F
L161P
156K
157K
164K
146R
118
120
122
124
[ppm]
8.6
8.2
7.8
7.4
[ppm]

Figure S11

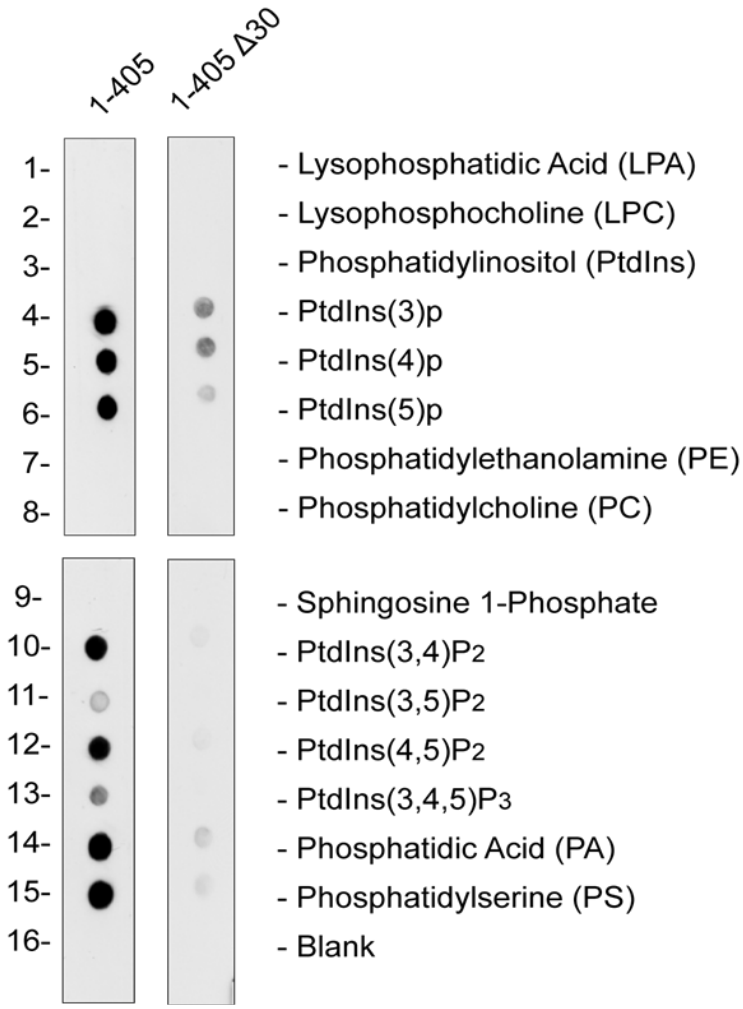
1-405
1-405 Δ30
1- - Lysophosphatidic Acid (LPA)
2- - Lysophosphocholine (LPC)
3- - Phosphatidylinositol (PtdIns)
4- - PtdIns(3)p
5- - PtdIns(4)p
6- - PtdIns(5)p
7- - Phosphatidylethanolamine (PE)
8- - Phosphatidylcholine (PC)
9- - Sphingosine 1-Phosphate
10- - PtdIns(3,4)P2
11- - PtdIns(3,5)P2
12- - PtdIns(4,5)P2
13- - PtdIns(3,4,5)P3
14- - Phosphatidic Acid (PA)
15- - Phosphatidylserine (PS)
16- - Blank

SUPPLEMENTARY METHODS

Expression of Recombinant Talin Polypeptides. The cDNA encoding murine talin residues 1-85 (F0), 86-202 (F1) and 1-202 (F0F1) were synthesized by PCR using a mouse talin1 cDNA as template, cloned into the expression vector pet-151TOPO (Novagen, Merck Biosciences, Nottingham) and expressed in *E.Coli* BL21 STAR (DE3) cultured in either LB for unlabelled protein, or in M9 minimal media for preparation of isotopically-labeled samples for NMR. Recombinant His-tagged talin polypeptides were purified by nickel-affinity chromatography following standard procedures. The His-tag was removed by cleavage with AcTEV protease (Invitrogen), and the proteins were further purified by anion-exchange (F0, F1, F0F1) or cation-exchange (F0-F3). F1-loop deletions were introduced into the DNA encoding talin residues 35-428 in pBluescript K5(+) using Inverse PCR followed by religation of the product. The deletion was confirmed by sequence analysis and the desired talin fragments were produced by PCR and cloned into pET151TOPO.

Lipid vesicle preparation. Small unilamellar vesicles (SUVs) for the NMR titrations were prepared by sonication. The lipid solutions in chloroform were mixed in required proportions and evaporated under a nitrogen stream. The film was dried overnight on a vacuum pump and the lipid re-suspended in MES buffer pH 6.1 at 25 mM by vortexing. The solution was sonicated on ice in short bursts until clear using a 50% duty cycle. The vesicles were spun on a bench-top centrifuge at 13,000 rpm for 3 min and the supernatant used for the titrations.

NMR Spectroscopy. NMR samples of all the protein constructs were prepared at 1mM in a phosphate buffer comprising 20mM sodium phosphate pH 6.5, 50mM NaCl, 2mM DTT with 10% (v/v) of $^{2}H_2O$. NMR spectra were obtained at 298K using Bruker AVANCE DRX 600 or AVANCE DRX 800 spectrometers both equipped with CryoProbes. Proton chemical shifts were referenced to external DSS. The ^{15}N and ^{13}C chemical shifts were referenced indirectly

using recommended gyromagnetic ratios (Wishart et al, 1995). Spectra were processed with TopSpin (Bruker) and analysed using Analysis (Vranken et al, 2005). 3D HNCO, HN(CA)CO, HNCA, HN(CO)CA, HNCACB and HN(CO)CACB experiments were used for the sequential assignment of the backbone NH, N, CO, $C\alpha$ and $C\beta$ resonances. Side chain assignments were obtained using 3D H(C)CH-TOCSY and (H)CCH-TOCSY experiments. Aromatic side chain assignments were obtained using ^{13}C-resolved 3D NOESY- HSQC.

For structural analysis of the synthetic loop peptide (residues 139-168), 1 mM samples were prepared in 20 mM MES buffer, pH 6.1 containing either 5% (v/v) of $^{2}H_2O$ or 35% (v/v) TFE-d_3 (Sigma-Aldrich). NMR spectra were obtained at 298K using Bruker AVANCE DRX 600 or AVANCE DRX 800 spectrometers both equipped with CryoProbes. Proton chemical shifts were referenced to the internal TSP standard introduced into the sample using a capillary insert (Sigma-Aldrich). The ^{1}H chemical shifts were assigned using 2D COSY-DQF, TOCSY (30 and 70 ms) and NOESY (100ms) spectra.

Peptide interactions with lipids were analysed using 0.1 mM solutions in 10 mM MES buffer pH 6.1 containing 5% (v/v) of $^{2}H_2O$. 2D COSY-DQF spectra were recorded at 298K for the free peptide and the peptide in the presence of 2 mM lipid added as SUVs. The F1 interactions with lipids were analysed using a 0.01 mM solution of uniformly ^{15}N-labelled F1 fragment or mutants thereof in 20 mM MES buffer, pH 6.1 containing 20 mM NaCl and 5% (v/v) of $^{2}H_2O$. 2D [^{1}H,^{15}N]-HSQC spectra were recorded at 298K for the free protein and the protein in the presence of 2 mM lipid added as SUVs. The spectra were processed and analysed using TopSpin 2.1 software (Bruker).

NMR Structure Calculations. Distance restraints were obtained from the following experiments: 3D ^{15}N-edited NOESY-HSQC (800 MHz, 100ms), ^{13}C-edited NOESY-HSQC (800MHz, 100ms) and ^{13}C-edited NOESY-HSQC (800MHz, 80ms) on aromatics. All

NOESY peaks were picked semi-automatically in Analysis with noise and artifact peaks removed manually. Cross-peak intensities were used to evaluate target distances. Dihedral restraints (Φ/Ψ) were obtained with TALOS software (Cornilescu et al, 1999). Hydrogen-bond restraints were incorporated based on the temperature dependence of NMR chemical shifts (Baxter et al, 1998) using a series of [^{1}H,^{15}N]-HSQC spectra collected from 15ºC-35ºC, and secondary structure elements identified from initial rounds of structure calculation. Residual ^{1}H,^{15}N dipolar couplings were measured in the presence of 8mg/ml Pf1 phage (Asla Ltd., Latvia) as the alignment medium (Hansen et al, 1998) using IPAP [^{1}H,^{15}N]-HSQC experiments (Ottiger et al, 1998). Couplings were evaluated using ANALYSIS and analysed with the program MODULE 1.0 (Dosset et al, 2001). Initial models were generated with CYANA using the CANDID (Herrmann et al, 2002) method for NOESY cross-peak assignment and calibration. These models were used as initial structures in structure calculations by Aria (Linge et al, 2001). The acceptance tolerances in the standard protocol of Aria 1.2 were modified to set violation tolerances to 5.0, 2.0, 1.0, 0.5, 2.0, 0.5, 0.1Å for iterations 2-8, respectively, with iteration 1 containing the initial models. Any cross-peaks rejected by Aria were checked manually and those found to be reliable were added to the calculation. 200 structures were calculated at each iteration, the 20 lowest energy structures retained and 10 used for final restraint analysis. The 30 lowest energy structures from iteration 8 were further refined in the presence of explicit water molecules. The structural statistics for each domain are presented in: Table 1, F0; Table 2, F1; Table 3, F0F1.

Secondary structure of the F1 loop peptide was assessed from the NOE patterns in 2D NOESY (100ms) spectra and $^{1}H^{\alpha}$ chemical shift values. Distance NOE restraints for the structure calculations were obtained from 2D NOESY spectra (100 ms). Peptide structure was calculated using the standard Aria 1.2 protocol (Linge et al, 2001). 200 structures were

calculated at each iteration, the 30 lowest energy structures from iteration 8 were further refined in the presence of explicit water molecules, and 20 structures used for the analysis.

CD spectroscopy. The experiments were carried out at 20°C on a JASCO J-715 spectropolarimeter equipped with a JASCO PTC-348WI temperature control unit. The peptide was at 0.3 mg/ml in 20 mM MES buffer pH 6.1. The contribution of the lipids was removed from the spectrum by subtracting the spectrum of the lipid without the peptide.

Phospholipid Binding using PIP strips. Phosphatidylinositol phosphate strips (Invitrogen) were treated at room temperature for 5 h with 3% ovalbumin in TBS-T (10 mM Tris, pH 8.0, 150 mM NaCl, 0.1% Tween 20) to eliminate non-specific binding, and incubated overnight at 4 °C with His-tagged talin polypeptides (1 μg/ml) in TBS-T containing 3% ovalbumin. After incubation, the strips were washed three times at room temperature in TBS-T containing 0.1% ovalbumin, and talin binding was detected with a mouse anti-His horseradish peroxidase-conjugated antibody (ratio 1:6000, 1 h at room temperature, Alpha Diagnostics), followed by three washes in TBS-T. The signals were detected by enhanced chemiluminescence (Pierce).

Analysis of Integrin Activation. The activation state of endogenous α5β1 was assessed by measuring the binding of a recombinant soluble integrin-binding fragment of fibronectin (FN9–11) in three-color flow cytometric assays as described previously (Calderwood et al, 2004; Tadokoro et al, 2003). In experiments on CHO cells the α5β1 integrin expression was assessed in parallel by staining with PB1 (Brown & Juliano, 1985). Briefly, CHO cells were transfected with the indicated cDNAs using Lipofectamine (Invitrogen), and 24 h later cells were suspended and incubated with biotinylated recombinant GST-FN9–11 in the presence or absence of integrin inhibitors. For each preparation of biotinylated GST-FN9–11 the effective concentration was determined by titration. Cells were washed and bound FN9–11 detected

with Allophycocyanin (APC)-conjugated streptavidin. Binding of FN9–11 to gated transfected (GFP-positive) cells was assessed on a FACSCalibur instrument (BD Biosciences). The activation index was defined as AI = (F - F_o)/($F_{integrin}$) where F is the geometric mean fluorescence intensity (GMFI) of FN9–11 binding, F_o is the GMFI of FN9–11 binding in presence of EDTA, and $F_{integrin}$ is the standardized ratio of PB1 binding to transfected cells. $F_{integrin}$ expression ratio was defined for expressing cells as follows: $F_{integrin}$ = (F_{trans})/($F_{untrans}$), where F_{trans} is the geometric GMFI of PB1 binding to double expressing cells, and $F_{untrans}$ is the GMFI of PB1 binding to untransfected cells.

The activation state of αIIbβ3 integrins was assessed by measuring the binding of the ligand mimetic anti-αIIbβ3 monoclonal antibody PAC1 in three-color flow cytometric assays as described previously (Calderwood et al, 2004; Calderwood et al, 1999; O'Toole et al, 1995; Tadokoro et al, 2003). CHO cell lines stably expressing αIIbβ3 (Hughes et al, 1997; O'Toole et al, 1994) were transfected as described above and 24 h later cells were suspended and stained with PAC1. Cells were washed and bound PAC1 was detected with Alexa647-conjugated goat anti-mouse IgM (Southern Biotech). PAC1 binding to live, transfected (GFP-positive) cells was assessed. Activation was quantified and an activation index calculated as defined by the formula AI = (F – F0)/(Fmax – F0), where F is the GMFI of PAC1 binding, F0 is the GMFI of PAC1 binding in presence of EDTA, and Fmax is the GMFI of PAC1 binding in the presence of 2 μM Mn^{2+}.

SUPPLEMENTARY REFERENCES

Baxter NJ, Hosszu LL, Waltho JP, Williamson MP (1998) Characterisation of low free-energy excited states of folded proteins. *J Mol Biol* **284**: 1625-1639.

Brown PJ, Juliano RL (1985) Selective inhibition of fibronectin-mediated cell adhesion by monoclonal antibodies to a cell-surface glycoprotein. *Science* **228**: 1448-1451.

Calderwood DA, Tai V, Di Paolo G, De Camilli P, Ginsberg MH (2004) Competition for talin results in trans-dominant inhibition of integrin activation. *J Biol Chem* **279**: 28889-28895.

Calderwood DA, Zent R, Grant R, Rees DJ, Hynes RO, Ginsberg MH (1999) The Talin head domain binds to integrin beta subunit cytoplasmic tails and regulates integrin activation. *J Biol Chem* **274**: 28071-28074.

Cornilescu G, Delaglio F, Bax A (1999) Protein backbone angle restraints from searching a database for chemical shift and sequence homology. *J Biomol NMR* **13**: 289-302.

Dosset P, Hus JC, Marion D, Blackledge M (2001) A novel interactive tool for rigid-body modeling of multi-domain macromolecules using residual dipolar couplings. *J Biomol NMR* **20**: 223-231.

Hansen MR, Mueller L, Pardi A (1998) Tunable alignment of macromolecules by filamentous phage yields dipolar coupling interactions. *Nat Struct Biol* **5**: 1065-1074.

Herrmann T, Guntert P, Wuthrich K (2002) Protein NMR structure determination with automated NOE-identification in the NOESY spectra using the new software ATNOS. *J Biomol NMR* **24**: 171-189.

Hughes PE, Renshaw MW, Pfaff M, Forsyth J, Keivens VM, Schwartz MA, Ginsberg MH (1997) Suppression of integrin activation: a novel function of a Ras/Raf-initiated MAP kinase pathway. *Cell* **88**: 521-530.

Linge JP, O'Donoghue SI, Nilges M (2001) Automated assignment of ambiguous nuclear overhauser effects with ARIA. *Methods Enzymol* **339**: 71-90.

O'Toole TE, Katagiri Y, Faull RJ, Peter K, Tamura R, Quaranta V, Loftus JC, Shattil SJ, Ginsberg MH (1994) Integrin cytoplasmic domains mediate inside-out signal transduction. *J Cell Biol* **124**: 1047-1059.

O'Toole TE, Ylanne J, Culley BM (1995) Regulation of integrin affinity states through an NPXY motif in the beta subunit cytoplasmic domain. *J Biol Chem* **270**: 8553-8558.

Ottiger M, Delaglio F, Bax A (1998) Measurement of J and dipolar couplings from simplified two-dimensional NMR spectra. *J Magn Reson* **131**: 373-378.

Tadokoro S, Shattil SJ, Eto K, Tai V, Liddington RC, de Pereda JM, Ginsberg MH, Calderwood DA (2003) Talin binding to integrin beta tails: a final common step in integrin activation. *Science* **302**: 103-106.

Vranken WF, Boucher W, Stevens TJ, Fogh RH, Pajon A, Llinas M, Ulrich EL, Markley JL, Ionides J, Laue ED (2005) The CCPN data model for NMR spectroscopy: development of a software pipeline. *Proteins* **59**: 687-696.

Wishart DS, Bigam CG, Yao J, Abildgaard F, Dyson HJ, Oldfield E, Markley JL, Sykes BD (1995) 1H, 13C and 15N chemical shift referencing in biomolecular NMR. *J Biomol NMR* **6**: 135-140.

SUPPLEMENTARY FIGURES

Supplementary Figure 1: (**A**) [^{1}H,^{15}N]-HSQC spectrum of the F0F1 (residues 1-202) double domain (Black) overlaid with the spectra of F0 (red) and F1 (blue) alone. Insert: The tryptophan indole region of the spectrum shows a large change in chemical shift of the F0 tryptophan (W61) between F0 and F0F1. (**B**) Chemical shift changes (>0.05 ppm) between the individual domains and the F0F1 double domain are mapped (white) onto the surfaces of F0 (green) and F1 (blue). The two domains are oriented as they are in the F0F1 structure. The changes map onto the interface between the two domains.

Supplementary Figure 2: The F0 domain of talin is highly conserved and has similar properties to Ras-association domains. (**A**) Sequence alignment of mouse talin1 residues 1-86 with the corresponding regions of other talins. Magenta – invariant residues; yellow - residues that are highly conserved. The secondary structure elements are shown above the alignments. The sequences used are; talin1 of mouse (P26039), human (Q9Y490) and chicken (P54939); talin2 of mouse (Q71LX4) and human (Q9Y4G6); talin of *Drosophila* (Q9VSL8), zebrafish (Q7SY14) and mosquito (Q7QJE3). (**B**) Electrostatic surface of talin1 F0. (**C**) Electrostatic surface of the Ras-binding domain of Raf – the orientation is the same as for talin1 F0 shown in (B). (**D**) Electrostatic surface of the Ras-binding domains of RalGDS – the orientation is the same as for talin1 F0 shown in (B). (**E**) [^{1}H,^{15}N]-HSQC spectra of F0 in the absence (blue) and presence (red) of GMP.PNP Rap1 at 1:3 molar ratio. (**F**) Titration curves for the interaction of F0 with GMP.PNP Rap1 (red) and GDP Rap1 (blue). Dissociation constants were measured for multiple residues and a typical binding curve, obtained from Glycine 11, is shown here. Dissociations constants (Kd) of 140 μM for GMP.PNP Rap1 and 700 μM for GDP-Rap1 were determined by the least square analysis of the titration data

Supplementary Figure 3: (**A**) Regions of the [^{1}H,^{15}N]-HSQC spectra of F0 and F1, and the F0F1 double domain showing cross-peaks corresponding to arginine N$^{\varepsilon}$H-groups. The side-chain N$^{\varepsilon}$H cross-peak of R181 (indicated by a *) is observed only in the F0F1 fragment, in agreement with the formation of the salt-bridge involving the side-chain. (**B**) Strips of the ^{15}N-NOESY-HSQC spectra showing the NOEs involving W61 N$^{\varepsilon 1}$H and R181 N$^{\varepsilon}$H protons, indicating their close proximity at the F0-F1 interface illustrated in Figure 2E. Similarly, large numbers of intra- and inter-domain NOEs were detected for all arginine N$^{\varepsilon}$H-groups at the interface, in agreement with their role in stabilising the relative domain orientation.

Supplementary Figure 4: The talin F1-loop is disordered in the whole head. [^{1}H-^{15}N] HSQC spectrum of residues 1-405 with the assignments of the F1-loop transferred onto it. All positions of the loop resonances in the F1 fragment correspond to the sharp intense signals in the spectrum of the whole head, indicating the highly dynamic properties of the loop region.

Supplementary Figure 5: The closest structural homologues of talin F0 and F1; (**A**) Talin1 F0 (**B**) ISG15 (1z2m), (**C**) ubiquitin (1ubi) and (**D**) RalGDS (1lfd). The proteins have the same orientations as F0 in (A).

Supplementary Figure 6: [^{1}H,^{15}N]-HSQC spectrum of the F1 domain (residues 86-202) (black) overlaid with the F1-loop deletion mutants; Δ30 (Δ D139-D168) (red), Δ31 (Δ K138-D168) (light blue) and Δ34 (Δ K137-E170) (green).

Supplementary Figure 7: (**A**) Correlation between experimental residual dipolar couplings (RDC) and calculated couplings for the NMR structure of the F0F1 double domain. All RDC values are in agreement with a single alignment tensor for F0F1(Δ30), confirming the fixed relative orientation of the domains. The blue lines represent the Chi^{2} value for each fit. (**B**)

SAXS experimental scattering profile of F0F1(Δ30) compared with the *ab initio* shape reconstructed using GASBOR (red line).

Supplementary Figure 8: (**A**) Sequence alignment of the mouse talin1 F1 loop (residues 133-170) with the corresponding regions of other talins. Magenta – invariant residues; yellow - residues that are highly conserved. The sequences used are; talin1 of mouse (P26039), human (Q9Y490), chicken (P54939) and zebrafish (Q5U7N6); talin2 of mouse (Q71LX4) and human (Q9Y4G6); talin of mosquito (Q8K1B8) and drosophila (Q9VSL8). (**B**) Helical Wheel representation of the F1-loop. The side of the helix oriented to the top is predominantly basic in charge. (**C**) H^N/H^N region of 2D NOESY spectra of the loop peptide in aqueous buffer (left) and in buffer containing 35% TFE (right) illustrating sequential H^N/H^N connectivities characteristic of a helical structure. (**D**) NOE connectivities and deviation of the $^1H^\alpha$ chemical shifts from the random coil values detected for the F1 loop peptide in aqueous buffer (left) and in buffer containing 35% TFE (right).

Supplementary Figure 9: The effect of POPC, 1:4 POPS:POPC and 1:19 PIP2:POPC SUVs on the [^{1}H,^{15}N]-HSQC spectra of F1. (**A**) F1 in the presence of 6 mM PIP2:POPC. (**B**) Superposition of the F1 spectra in the free form (green) and in the presence of 6 mM 1:4 POPS:POPC (black). (**C**) Superposition of the F1 spectra in the free form (green) and in the presence of 6 mM 1:19 PIP2:POPC (black). In (B) and (C) the signals in the bound state are broadened out beyond detection; the residual signals correspond to the strongest resonances from the small fraction of unbound protein. (**D**) Superposition of ^{1}H projections of F1 spectra in A and B illustrating the reduction in resonance intensities in the presence of POPS (red) and PIP2 (black), but not pure POPC (blue). All spectra were recorded under the same conditions. The same contour levels were used for the 2D spectra and the same scaling factor for the 1D projections.

Supplementary Figure 10: Comparison of the effect of 1:4 POPS:POPC SUVs on the [^{1}H,^{15}N]-HSQC spectra of and cosedementation of F1 mutants. (**A**) Superposition of the F1 spectra in the free form (green) and in the presence of 6 mM 1:4 POPS:POPC (black) for the F1(M158G/E159G/L161G) mutation that destabilises the transient helix in the F1 loop. (**B**) Superposition of the F1 spectra in the free form (red) and in the presence of 6 mM 1:4 POPS:POPC (blue) for F1(L161P) mutation that destabilises the transient helix in the F1 loop. (**C**) Superposition of ^{1}H projections from (A) illustrating the reduction in resonance intensities in the presence of POPS. Note that the relative intensities of the residual signals are higher than for the wild type under the same conditions (Figure S10), corresponding to a reduced affinity of the interaction. (**D**) Superposition of ^{1}H projections in (B) illustrating similar resonance intensities in the presence of POPS and in the free form. The presence of the lipid induces selective broadening and chemical shift changes in a small number of resonances, corresponding to a localised interaction with lower affinity than for the wild type. (**E**) Association of F1 and its mutants with 1:4 POPS:POPC SUVs as measured by a co-sedimentation assay. Supernatant (S) and pellet (P). Top – Lanes 1, 2 – wild type; 3, 4 - F1(Δ30); 5, 6 - F1(R146E,R153E,K156E); 7, 8 – F1(M158P); 9, 10 – F1(M158P/E159G); 11, 12 - F1(M158S/E159S/L161S); 13, 14 – F1(L161P). Bottom: fraction of lipid-bound protein estimated from the band density using ImageJ. Incubation time 1h. (**F**) Expansion of the spectrum in (B) illustrating the effect of the SUVs on the signals of the positively charged residues within the F1 loop. Note that all the spectral changes are localised within the loop region that can be identified by strong sharp signals.

Supplementary Figure 11: The F1-loop binds to negatively charged lipids. Binding of His-tagged talin head polypeptides (residues 1-405) to phosphatidylinositol phosphate strips containing an array of acidic phospholipids (Invitrogen) was detected using an anti-His antibody. Each *spot* contains 100 pmol of phospholipid, and the membrane was probed with

1μg/ml protein. Each experiment was done in triplicate. The talin1 head binds to several phospholipids, whereas talin1 head minus the loop (Δ30) showed a large decrease in binding.

SUPPLEMENTARY TABLES

Table 1. Solution Structure Determination of Talin 1-85	
Experimental restraints	
Restraints	
Unique/Ambiguous NOEs	2242/107
Intraresidue	951/22
Sequential	486/23
Short range (1< [i – j] <5)	246/16
Long range ([i – j] >4)	559/46
φ/ψ dihedral angles[a]	108
Energies (Kcal mol^{-1})[b]	
Total	-3522 ± 81
Van Der Waals	-827 ± 8
NOE	31 ± 4
RMS deviations[b]	
NOEs (Å) (no violations > 0.5 Å)	0.016 ± 0.001
Dihedral restraints (º) (no violations > 5º)	0.30 ± 0.08
Bonds (Å)	0.0035 ± 0.0001
Angles (º)	0.46 ± 0.01
Impropers (º)	1.36 ± 0.07
Ramachandran map analysis[c]	
Allowed regions	91.3%
Additional allowed regions	8.2%
Generously allowed regions	0.1%
Disallowed regions	0.3%
Pairwise rms difference (Å)[d]	
Residues 3-85	0.57 (1.02)
Regions of secondary structure	0.47 (0.95)

[a] From chemical shifts using Talos.
[b] Calculated in ARIA 1.2 for the 20 lowest energy structures refined in water.
[c] Obtained using PROCHECK-NMR.
[d] For backbone atoms; value for all heavy atoms in brackets.

Table 2. Solution Structure Determination of Talin 86-202	
Experimental restraints	
Restraints	
Unique/Ambiguous NOEs	2214/92
Intraresidue	1050/44
Sequential	515/24
Short range (1< [i – j] <5)	251/5
Long range ([i – j] >4)	398/19
φ/ψ dihedral angles[a]	56
Energies (Kcal mol^{-1})[b]	
Total	-4605.01 ± 167.02
Van Der Waals	-1053.62 ± 16.73
NOE	53.38 ± 12.77
RMS deviations[b]	
NOEs (Å) (no violations > 0.5 Å)	0.02 ± 0.001
Dihedral restraints (º) (no violations > 5º)	0.41 ± 0.14
Bonds (Å)	0.004 ± 0.0001
Angles (º)	0.57 ± 0.01
Impropers (º)	1.61 ± 0.08
Ramachandran map analysis[c]	
Allowed regions	80.4%
Additional allowed regions	15.0%
Generously allowed regions	2.7%
Disallowed regions	1.9%
Pairwise rms difference (Å)[d]	
Residues 88-196	6.66 (7.12)
Regions of secondary structure	0.91 (1.48)

[a] From chemical shifts using Talos.
[b] Calculated in ARIA 1.2 for the 20 lowest energy structures refined in water.
[c] Obtained using PROCHECK-NMR.
[d] For backbone atoms; value for all heavy atoms in brackets.

Table 3. Solution Structure Determination of Talin 1-202	
Experimental restraints	
Restraints	
Unique/Ambiguous NOEs	5704/902
Intraresidue	2055/249
Sequential	1319/180
Short range (1< [i – j] <5)	817/126
Long range ([i – j] >4)	1513/347
φ/ψ dihedral angles[a]	124
RDCs	66
Energies (Kcal mol^{-1})[b]	
Total	-5774 ± 77
Van Der Waals	-717 ± 23
NOE	124 ± 9
RDC	10.3 ± 0.1
RMS deviations[b]	
NOEs (Å) (no violations > 0.5 Å)	0.019 ± 0.001
Dihedral restraints (º) (no violations > 5°)	1.14 ± 0.11
Bonds (Å)	0.0042 ± 0.0001
Angles (º)	0.55 ± 0.01
Impropers (º)	1.56 ± 0.1
Ramachandran map analysis[c]	
Allowed regions	84.3%
Additional allowed regions	13.8%
Generously allowed regions	1.0%
Disallowed regions	0.9%
Pairwise rms difference (Å)[d]	
Residues 3-195	0.57 (0.84)
Regions of secondary structure	0.43 (0.68)

[a] From chemical shifts using Talos.
[b] Calculated in ARIA 1.2 for the 20 lowest energy structures refined in water.
[c] Obtained using PROCHECK-NMR.
[d] For backbone atoms; value for all heavy atoms in brackets.